

# Measuring Solar Differential Rotation with an Iterative Phase Correlation Method

Zdeněk Hrazdíra 6, Miloslav Druckmüller, and Shadia Habbal 6

<sup>1</sup> Institute of Mathematics, Faculty of Mechanical Engineering, Brno University of Technology, 616 69 Brno, Czech Republic; hrazdira.zdenek@google.com
<sup>2</sup> Institute for Astronomy, University of Hawaii, Honolulu, HI 96822, USA

\*\*Received 2020 June 10; revised 2020 October 29; accepted 2020 October 29; published 2020 December 23

#### **Abstract**

A reliable inference of the differential rotation rate of the solar photosphere is essential for models of the solar interior. The work presented here is based on a novel iterative phase correlation technique, which relies on the measurement of the local shift, at the central meridian, between two images separated by a given time interval. Consequently, it does not require any specific reference features, such as sunspots or supergranules, nor extended observations spanning several months. The reliability of the method is demonstrated by applying it to high spatial and temporal resolution continuum images of the solar photosphere, at 6173 Å, acquired by the Solar Dynamics Observatory Helioseismic and Magnetic Imager over one complete Carrington rotation. The data selected covers the time period of 2020 January 1 to February 2. The method was applied to one day, and to the full time interval. The differential rotation rate derived using this feature-independent technique yields values that fall in the middle of the range of those published to date. Most importantly, the method is suited for the production of detailed rotation maps of the solar photosphere. It also enables the visual and quantitative identification of the north–south asymmetry in the solar differential rotation rate, when present.

*Unified Astronomy Thesaurus concepts:* Solar rotation (1524); Solar differential rotation (1996); Astronomical techniques (1684); Astronomical models (86); Analytical mathematics (38); Computational methods (1965); Direct imaging (387); Astronomy (80); Astronomical methods (1043); Astronomy software (1855); Astronomy data analysis (1858); Astronomy data visualization (1968)

#### 1. Introduction

The identification of sunspots with features on the solar surface led to the discovery of solar rotation in the 17th century, and the variation of the rotation speed with latitude, or the differential rotation rate, by Scheiner (1630). Advances in observational tools over the centuries led to the discovery of the oscillation modes of the Sun (Leighton et al. 1962), which established the field of helioseismology (see the review by Leibacher et al. 1985). Helioseismology further revealed that the differential rotation rate changes with depth in the convection zone (Thompson et al. 1996). Given that the differential rotation rate is now established as a necessary mechanism for generating solar magnetic fields, i.e., the solar dynamo (Elsässer 1950; Babcock & Babcock 1955; Parker 1955), the accurate determination of the differential rotation rate, starting from the solar surface, becomes even more compelling.

Recently Beck (2000) compared the differential rotation rates derived from the most widely used techniques, namely the Doppler shifts of photospheric spectral lines, the Doppler feature tracking, the magnetic feature tracking and the p-mode splittings. He found a large disparity in the values inferred from these different techniques. The difficulties hampering the accuracy of the measurement are directly linked to the complexity of observed features on the solar surface itself. Additional limitations due to foreshortening effects close to the poles limit the viability of these techniques to low latitudes. Sunspot tracking adds to the limitation, since they are rarely observed above 30° latitude. Furthermore, since all tracked features, such as sunspots, supergranules and granules, for example, are subject to intrinsic temporal variability, they will inevitably bias any measurement of rotation rate.

The goal of this paper is to show how the iterative phase correlation technique, recently developed by Hrazdíra et al. (2020)

can be applied to continuum images of the photosphere to derive a reliable, feature-independent, solar differential rotation rate. This method belongs to the class of tracer measurement methods. In the past, the cross-correlation method applied to images of the solar photosphere had already been used for that purpose (Beck 2000). The phase correlation technique was first introduced by Kuglin & Hines (1975) for the alignment of displaced images taken with different imaging devices or under varying conditions of illumination. It has been successfully implemented by Druckmüller (2009) for the alignment of total solar eclipse images taken with different exposure times and different optics, and has rendered images with unprecedented detail (see, e.g., Druckmüller et al. 2014).

The best data available at present for the implementation of this technique are the 6173 Å data from the Helioseismic and Magnetic Imager (HMI) instrument on the Solar Dynamics Observatory (SDO) (Lemen et al. 2011), provided by the Joint Science Operations Center (http://jsoc.stanford.edu), which represent emission from the photosphere (see Lemen et al. 2011, Table 1). The technique is described in Section 2. The results emerging from the application of this technique to one Carrington rotation of SDO/HMI data are presented in Section 3, where the differential rotation rate thus derived is compared with inferences from a number of different techniques. Also demonstrated in that section is how the technique recovers the now well-established north—south asymmetry of the solar differential rotation rate. The results are summarized in Section 5 together with some concluding remarks.

### 2. Measurement Technique

## 2.1. Basics of the Technique

In this work, the inference of the solar rotational speed at different latitudes is achieved by measuring the local west–east

Table 1
Trigonometric Flow Speed Coefficients

•	-		
Flow Speed Curve Type	A	В	<i>C</i>
W–E (B) (1 month)	14.21	-1.61	-2.89
W–E (B) (1 day)	14.27	-1.46	-2.66
W–E (N) (1 month)	14.20	-1.93	-2.75
W-E (N) (1 day)	14.26	-1.24	-3.47
W–E (S) (1 month)	14.23	-1.28	-3.02
W–E (S) (1 day)	14.28	-1.68	-1.84
N–S (N) (1 month)	0.01	-0.82	8.18
N–S (N) (1 day)	-0.01	-0.62	7.40
N–S (S) (1 month)	-0.14	0.61	-5.84
N–S (S) (1 day)	-0.27	1.29	-7.57

**Note.** The table includes best (least-squares) fitting coefficients A, B, C for different types of west-east (W-E) and north-south (N-S) trigonometric flow speed profile fits for northern (N), southern (S) or both (B) hemispheres, obtained from both one month and one day data sets in degrees per day according to Equation (12).

and north–south image shifts  $\Delta x$ ,  $\Delta y$  between pairs of SDO/HMI continuum full-disk 4096 × 4096 images with time step  $\Delta t$  by means of image registration (see Figure 1). Measured image shifts are then projected onto the solar surface, allowing the corresponding angular shifts  $\Delta \varphi_x$ ,  $\Delta \varphi_y$  to be found. The average angular velocities  $\omega_x$  and  $\omega_y$  are then calculated based on the time difference  $\Delta t$  between the two images following the relations:

$$\omega_x = \frac{\Delta \varphi_x}{\Delta t},\tag{1}$$

$$\omega_{y} = \frac{\Delta \varphi_{y}}{\Delta t},\tag{2}$$

where the time difference  $\Delta t$  is determined by the SDO/HMI continuum instrument temporal cadence  $\Delta_t$  and the difference between the image indices  $\Delta_p$ , namely

$$\Delta t = \Delta_p \Delta_t. \tag{3}$$

The SDO/HMI temporal cadence is constant ( $\Delta_t = 45$  s). Pairs of consecutive images ( $\Delta_p = 1$ ) are used to ensure the best signal-to-noise ratio for the image registration and thus achieve a high-precision measurement of the image shifts  $\Delta x$  and  $\Delta y$ .

# 2.2. Time Step Choice

The accuracy and reliability of the image registration technique depends heavily on the chosen time step  $\Delta t$ . As mentioned in the previous section, a time step of 45 s is used for all the measurements throughout the article. The reasoning behind this choice can be seen visually in Figures 2 and 3. Since the SDO/HMI images mostly contain information about the granulation on the solar surface (see Figures 1(a) and (b)), the time difference between the two pictures is limited by the lifetime of these granules. A typical granule has a lifetime of around 10–15 minutes, which limits the time step to around 4 minutes, to still keep good overlap and correlation between the

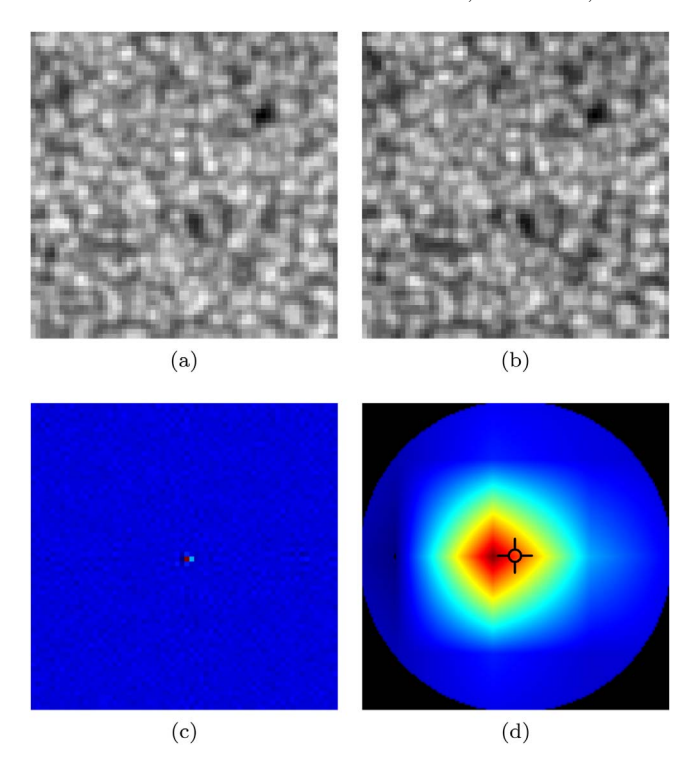


**Figure 1.** High-precision subpixel image shift estimation via iterative phase correlation on a pair of  $64 \times 64$  pixel SDO/HMI image subregions with time step  $\Delta t = 45$  s. (a) First input image, (b) second input image, (c) heat map of the phase correlation landscape computed from the two input images (with higher values corresponding to warmer colors), (d) circularly cropped heat map of the bilinearly upscaled neighborhood around the location of maximal phase correlation with marked center of gravity (centroid) location.

images. The lowest possible time step of 45 s is thus chosen to maximize the signal-to-noise ratio. Figure 2 shows how the image shift measurement becomes consistently highly unreliable with time steps larger than 4 minutes, while Figure 3 visualizes the phase correlation maximum peak quality degradation with larger time steps—note the sharp decline of the maximum phase correlation values from (a) to (c).

#### 2.3. The Image Registration Algorithm

The local image shifts were calculated for a chosen set of pixel coordinates (and their neighborhoods) by the iterative phase correlation (IPC) high-precision subpixel image registration algorithm (Hrazdíra et al. 2020). As the vast majority of west–east shifts between pairs of consecutive ( $\Delta t = 45 \text{ s}$ ) images lie in the interval [0.1, 0.2] pixel, the high subpixel precision of the IPC algorithm justifies the choice of the method. Given that the IPC method was recently developed by the authors of this article, its main advantages and limitations were well known and were taken into account during the entire differential rotation estimation process. The main relevant advantage of the IPC algorithm is the potential for very high subpixel spatial accuracy with correct parameters, due to its iterative nature. These parameters can be optimized beforehand for a given type of image (different sizes, different amounts of noise, etc.). The main limitation of the technique is the amount of noise present in the images and the magnitude of the shift between them. Naturally, with higher noise levels, the method starts to lose its subpixel accuracy. Similarly, with larger image shifts, the amount of overlap between the two images starts to diminish, which also hinders the quality of the correlation

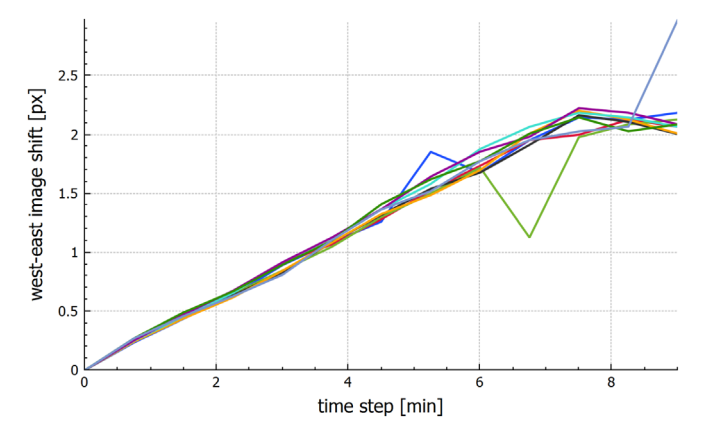


**Figure 2.** West–east image shifts measured by the IPC algorithm for multiple pairs of SDO/HMI images with different time steps  $\Delta t$ . Each curve represents a different random first image.

landscape and thus lowers the accuracy of the resulting measured image shift. Both of these limiting effects are minimized by choosing a very short time step.

For each of the registered pixels, two equal-sized square neighborhoods (subregions) are selected from each of the two SDO/HMI images at equal locations relative to the image reference pixel [ $x_{mid}$ ,  $y_{mid}$ ], defined in the header of each SDO/ HMI flexible image transport system (FITS) file. This way, changes in the image coordinates of the solar center caused by movements of the SDO are taken into account and do not degrade the results. Since the time interval between the correlated images is only 45 s, all such changes are negligible in comparison with the measured image shift. Median absolute shift of the solar center was measured at approximately 0.005 pixel in both directions (both according to the FITS file header and according to measurements by the IPC method). The corresponding image subregion pairs are then iteratively phase correlated, yielding the pixel shift estimates  $\Delta x$  and  $\Delta y$ for each of the selected locations.

#### 2.4. Locations of the Image Shift Measurements

To reduce the effects of distortions arising due to the perspective projection of the 3D solar surface onto the 2D image, only pixels lying on the central meridian (and their small neighborhoods) were considered. This also allowed for the construction of a central meridian flow speed map, with solar latitude  $\theta$  on the vertical axis and time t (assuming the image pairs are ordered chronologically) on the horizontal axis. For each of the considered picture pairs, the central subregion pixels were distributed evenly across a portion of the central meridian, symmetrically around the central pixel  $[x_{mid}, y_{mid}]$ . The entire meridian (from  $\theta = -90^{\circ}$  to  $\theta = 90^{\circ}$ ) was not considered, given the noticeable distortions caused by the perspective projection of the solar surface near the geographic poles. We label the vertical pixel size of the limited meridional "field of view" as  $\Theta_{v}$ , the number of individual registered subregions on the meridian of each picture pair as M and index each of the subregions from north to south with the ascending index  $\mu$  (starting from zero). We further assume that the standard image coordinate system has the x coordinate (image column) increasing from left to right, and the y coordinate (image row) increasing from top to bottom. To only measure

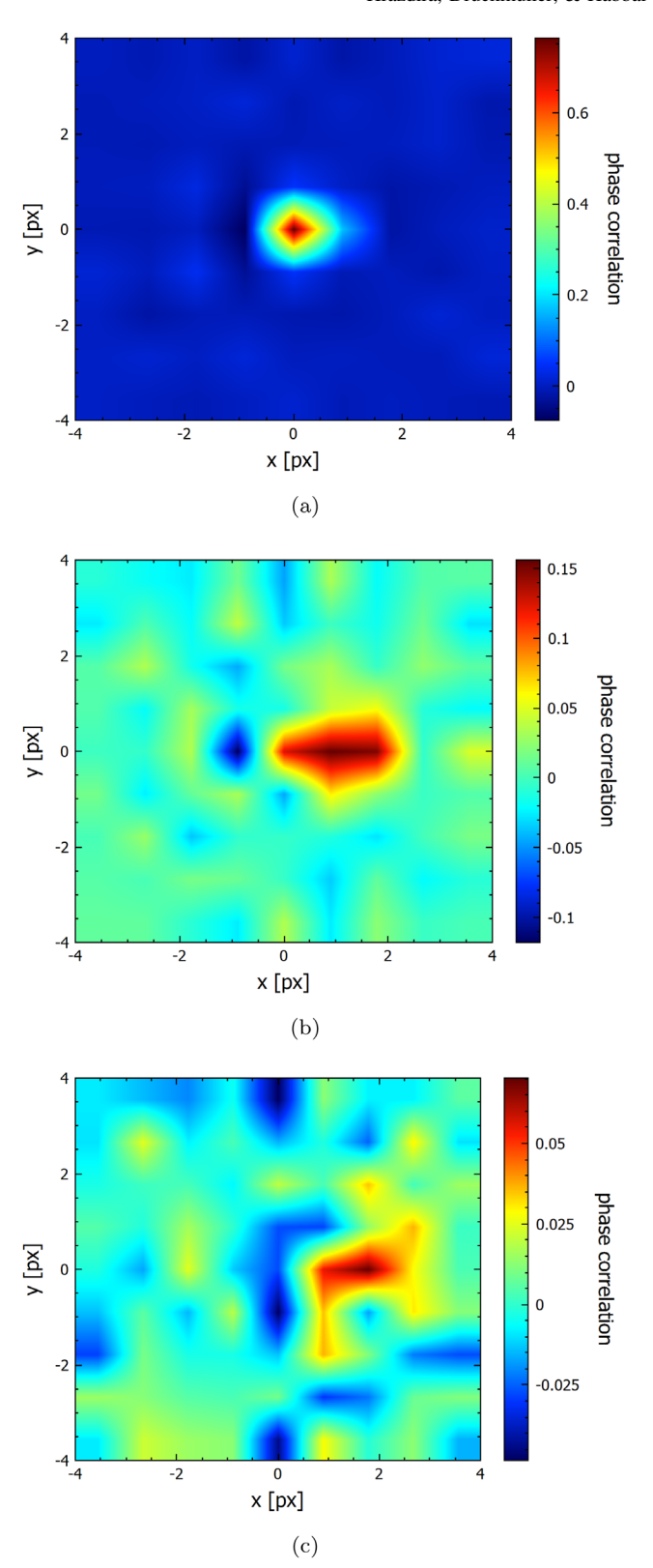


**Figure 3.** Zoomed in heat maps of bilinearly upscaled phase correlation landscapes with two  $64 \times 64$  pixel SDO/HMI images for different time steps:  $\Delta t = 45$  s (a),  $\Delta t = 225$  s (b),  $\Delta t = 450$  s (c). See the associated video of roughly 30 minutes of continuous SDO/HMI imagery at https://www.youtube.com/watch?v=2iR5Ax75Ax4. Note that the color ranges were minimum/maximum normalized for each landscape, which means that in (a) dark red corresponds to correlation values around 0.8, while in (c) the same color corresponds to values just around 0.07.

the shifts on the central meridian, the central horizontal pixel coordinates of each subregion  $x(\mu)$  need to be fixed for all images at

$$x(\mu) = x_{\text{mid}},\tag{4}$$

while the central vertical pixel coordinates of each subregion  $y(\mu)$  (satisfying the equidistant and symmetry conditions mentioned above) can be set as

$$y(\mu) = y_{\text{mid}} + \Delta_y \left( \mu - \left| \frac{M}{2} \right| \right), \tag{5}$$

where  $\Delta_y$  is the vertical spacing between the equidistant subregion centers and can be determined by

$$\Delta_{y} = \frac{\Theta_{y}}{M - 1}.$$
 (6)

The solar latitude  $\theta(\mu)$  can be trigonometrically derived for every meridional subregion index  $\mu$  as

$$\theta(\mu) = \arcsin\left(\frac{\Delta_y\left(\left\lfloor\frac{M}{2}\right\rfloor - \mu\right)}{R}\right) + \theta_0,\tag{7}$$

where the two newly introduced variables R and  $\theta_0$  denote the size of the solar radius in pixels and the latitude of the observer (instrument), and are both described in the SDO/HMI FITS file header. For the differential rotation measurement, the vertical field of view was chosen as  $\Theta_y = 3400$  pixel and the number of subregions as M = 851 (an odd number of subregions, assuring the existence of a central element). According to Equation (6), this results in a  $\Delta_y = 4$  pixel vertical spacing between the equidistant meridional central subregion pixels.

# 2.5. Orthographic Projection of the Image Shift

Since the SDO/HMI image is essentially a 2D perspective projection of the 3D solar surface, the measured meridional image shifts  $\Delta x(\mu)$  and  $\Delta y(\mu)$  (calculated by iteratively phasecorrelating pairs of image subregions with centers at pixel coordinates  $[x(\mu), y(\mu)]$  given by Equations (4) and (5)) need to be projected back onto the solar surface and transformed into the angular shifts  $\Delta \varphi_x(\mu)$  and  $\Delta \varphi_y(\mu)$ . Since the distance between the SDO and the Sun is  $\sim 200 R_s$ , the image projection was assumed orthographic (parallel projection lines orthogonal to the projection plane-point of perspective at infinite distance). As only the central meridian subregion shifts are calculated for every image pair, the following image shift back-projection equations depend only on the latitude information  $\theta(\mu)$  (given in Equation (7)) and can also be derived trigonometrically. These orthographic back projections transform the image pixel shifts  $\Delta x(\mu)$ ,  $\Delta y(\mu)$  into the angular shifts  $\Delta \varphi_{x}(\theta(\mu))$  and  $\Delta \varphi_{y}(\theta(\mu))$  given by

$$\Delta \varphi_{x}(\theta(\mu)) = \arcsin\left(\frac{\Delta x(\mu)}{R\cos(\theta(\mu))}\right),$$
 (8)

$$\Delta\varphi_{\mathbf{y}}(\theta(\mu)) = \theta(\mu) - \arcsin\left(\sin\left(\theta(\mu)\right) - \frac{\Delta y(\mu)}{R}\right). \tag{9}$$

# 2.6. Equations for the Image Shift-based Solar Angular Velocity

If we now combine six of the previously described equations —the general Equations (1) and (2) for the angular velocities  $\omega_x(\theta(\mu))$  and  $\omega_y(\theta(\mu))$ , Equation (3) for the temporal difference between the two images  $\Delta t$ , Equation (7) for the solar latitude  $\theta$  ( $\mu$ ) and the orthographic projection Equations (8) and (9) for the angular shifts  $\Delta \varphi_x(\theta(\mu))$  and  $\Delta \varphi_y(\theta(\mu))$ , we get the final equations for the estimated angular velocities  $\omega_x(\theta(\mu))$  and  $\omega_y(\theta(\mu))$  of a meridional pixel with index  $\mu$  (with pixel indexing as described in Section 2.4) in the form of

$$\omega_{x}(\mu) = \frac{1}{\Delta_{p}\Delta_{t}} \operatorname{arccsc}\left(\frac{R}{\Delta x(\mu)}\right) \times \cos\left(\operatorname{arcsin}\left(\frac{\Theta_{y}}{M-1}\frac{1}{R}\left(\left\lfloor\frac{M}{2}\right\rfloor - \mu\right)\right) + \theta_{0}\right)\right)$$
(10)

for the west-east solar angular velocity, and

$$\omega_{y}(\mu) = \frac{1}{\Delta_{p}\Delta_{t}} \left( \arcsin\left(\frac{\Delta_{y}\left(\left\lfloor\frac{M}{2}\right\rfloor - \mu\right)}{R}\right) + \theta_{0} - \arcsin\left(\sin\left(\frac{\Delta_{y}\left(\left\lfloor\frac{M}{2}\right\rfloor - \mu\right)}{R}\right) + \theta_{0}\right) - \frac{\Delta_{y}(\mu)}{R} \right) \right)$$

$$(11)$$

for the north-south solar angular velocity.

#### 3. Results

#### 3.1. Data Sets Used for the Measurement

The west–east and north–south solar angular velocities  $\omega_x(\theta)$  and  $\omega_y(\theta)$  were measured for two sets of P=1999 pairs of consecutive images. The first data set uniformly spans the time interval from 2020 January 1 to February 2. This period approximately equals one full solar revolution at the equator (where the flow is faster than average) and 80% of a revolution near the poles (where the flow is slower than average).

The second data set uniformly spans the time interval from 2020 January 1 to January 2. This period approximately equals 4% of a solar revolution at the equator and 3% of a revolution near the poles.

The duration of both data set intervals ( $\sim$ 1 day and  $\sim$ 1 month) were chosen deliberately to measure both the potentially interesting short-lived phenomena and also the overall rotational speed profile. The specific initial date of both data sets (2020 January 1) was chosen arbitrarily and is not in any way special—both image data sets show very "calm" behavior during this period, with almost no clearly discernible large-scale features, such as sunspots, present.

The size of the central meridional subregions, from which the image shifts were calculated, was set to  $256 \times 256$  pixels. This size proved to be large enough for good image registration

quality, and at the same time small enough to provide good spatial flow speed resolution.

#### 3.2. Flow Speed Maps

Since M subregions were equidistantly distributed among different latitudes on the central meridian of every picture and measurements for P picture pairs were made, very detailed 2D west—east and north—south central meridian flow speed maps with  $P \times M$  resolution could be constructed for each data set. These maps can be seen in Figures 4(a), (c), and (e).

Although the measured angular velocity clearly varies with time in a given latitude band, the temporally coherent angular velocity values in the flow speed maps demonstrate the good image registration quality. Measured from horizontally (temporally) adjacent image shifts, although being computed from entirely different pairs of images, they are very similar at each latitude, which is demonstrated by the existence of the clearly distinguishable coherent faster than average and slower than average flows in Figure 4(a).

The west–east and north–south image shift  $\Delta x(\theta)$ ,  $\Delta y(\theta)$  and angular velocity  $\omega_x(\theta)$ ,  $\omega_y(\theta)$  values from all the P image pairs were also averaged at each latitude, resulting in picture-pair averages  $\overline{\Delta x(\theta)}$ ,  $\overline{\Delta y(\theta)}$  (see Sections 3.3 and 3.4) and  $\overline{\omega_x(\theta)}$ ,  $\overline{\omega_y(\theta)}$  (see Section 3.5). The rather smooth characteristics of the average west–east and north–south image shift profiles  $\overline{\Delta x(\theta)}$  and  $\overline{\Delta y(\theta)}$  (see Figures 4(b), (d) and (f)) can serve as good indicators of the entire rotational speed measurement quality.

#### 3.3. West-East Image Shift Profile

Upon closer inspection of the average west-east image shift profiles obtained from both data sets, very coherent curves with very little noise can be seen. The profile obtained from the one day data set (Figure 4(b)) is somewhat more chaotic than that of the one month data set (Figure 4(d)), which is expected, as the profile captures local flows and events happening on timescale comparable to the entire data set time span. These events can be seen very clearly as reddish and blueish streaks in the flow speed maps of both data sets, showing regions of faster than average or slower than average flow, lasting approximately 8 hr. The shorter time span data set flow speed map shows individual flows in more detail, while the longer time span flow speed map demonstrates the practically constant duration and presence of these flows. The profile obtained from the longer time span data set is almost perfectly smooth, displaying the overall global average west-east rotational speed profile.

# 3.4. North-South Image Shift Profile

Although being roughly one order of magnitude less significant than its west-east counterpart ( $\sim$ 0.01 pixel compared to  $\sim$ 0.2 pixel), the measurement result of the average north-south image shift profile  $\Delta y(\theta)$  is also quite interesting. The north-south profile clearly shows more noisy behavior, which can be caused by being near the accuracy limit of the image registration precision. In the north-south part of the registration, the iterative phase correlation method is estimating north-south shifts around 0.01 pixel between two  $256 \times 256$  pixel images, and such shifts are very hard to estimate with higher precision. However, a very clear overall trend can still be seen in the average profile (see Figure 4(f)).

In the northern solar hemisphere, the flow seems to be southwards, in addition to the natural ( $\sim 20 \times \text{faster}$ ) eastwards

rotational flow. This southwards part of the flow gets more significant closer to the north pole, roughly following a cubic (or arcsine) trend. The north—south image shift profile appears to be very close to being central-symmetric, meaning that the flow appears to be southwards in the northern hemisphere and northwards in the southern hemisphere, resulting in an overall flow toward the equator in both hemispheres, which speeds up significantly near the poles.

#### 3.5. The Final Flow Speed Profiles

According to multiple studies (Zhang et al. 2015; Lamb 2017), the southern solar hemisphere seems to be rotating (slightly, but noticeably) faster, than the northern hemisphere. The usual westest flow trigonometric fit (denoted  $\omega^{\dagger}(\theta)$ ) of the form

$$\omega^{\dagger}(\theta) = A + B\sin^2(\theta) + C\sin^4(\theta) \tag{12}$$

is always zero-symmetric, since even powers of the function  $\sin(\theta)$  are always even, and thus cannot capture such north-south asymmetric behavior. This results in unnecessarily large curve-fitting errors if the flow speed profile is not separated into northern and southern parts. On the contrary, a polynomial fit of a second degree (denoted  $\omega_x^*(\theta)$ ) in the simple form of

$$\omega_{\mathbf{r}}^{*}(\theta) = a + b\theta + c\theta^{2} \tag{13}$$

can capture any northern–southern hemisphere asymmetries with much less error and with the same amount of fitting parameters. This fit is thus included in all the image shift and flow speed profile figures, where the flow speed is not separated into northern and southern parts.

As the average north-south image shift profile clearly trends toward a cubic, it is only natural to fit the resulting north-south flow speeds with a polynomial of a third degree in the simple form of

$$\omega_{\nu}^{*}(\theta) = a + b\theta + c\theta^{2} + d\theta^{3}. \tag{14}$$

The values of the fitting parameters *A*, *B*, *C* and *a*, *b*, *c*, *d* for all mentioned flow profiles in degrees per day for northern, southern, and both hemispheres together are provided in Tables 1 and 2. The final average west—east and north—south flow speed profiles, together with their corresponding polynomial fits (and together with profiles inferred by different techniques, for comparison, in the west—east case) can be seen in Figures 5(a) and (c).

Furthermore, for a better visualization of the north-south asymmetry of the resulting west-east and north-south flows, Figures 5(b) and (d) show the average flow profiles and their corresponding best least-squares trigonometric fits (according to Equation (12)) separately for each hemisphere, with absolute latitude on the horizontal axis.

#### 4. Discussion

## 4.1. Image Registration Techniques

There is a vast literature on the image registration problem in computer vision research. The Iterative Phase Correlation (IPC) method is one of the many subpixel extensions of the classical phase correlation method (Kuglin & Hines 1975). The method is mainly based on the upscaling of the phase correlation landscape, adaptable bandpass filtering of the cross-power spectrum and its iterative character, which iteratively refines the resulting image shift by computing weighted centroids on a small region of interest (ROI) around the phase correlation peak in each iteration,

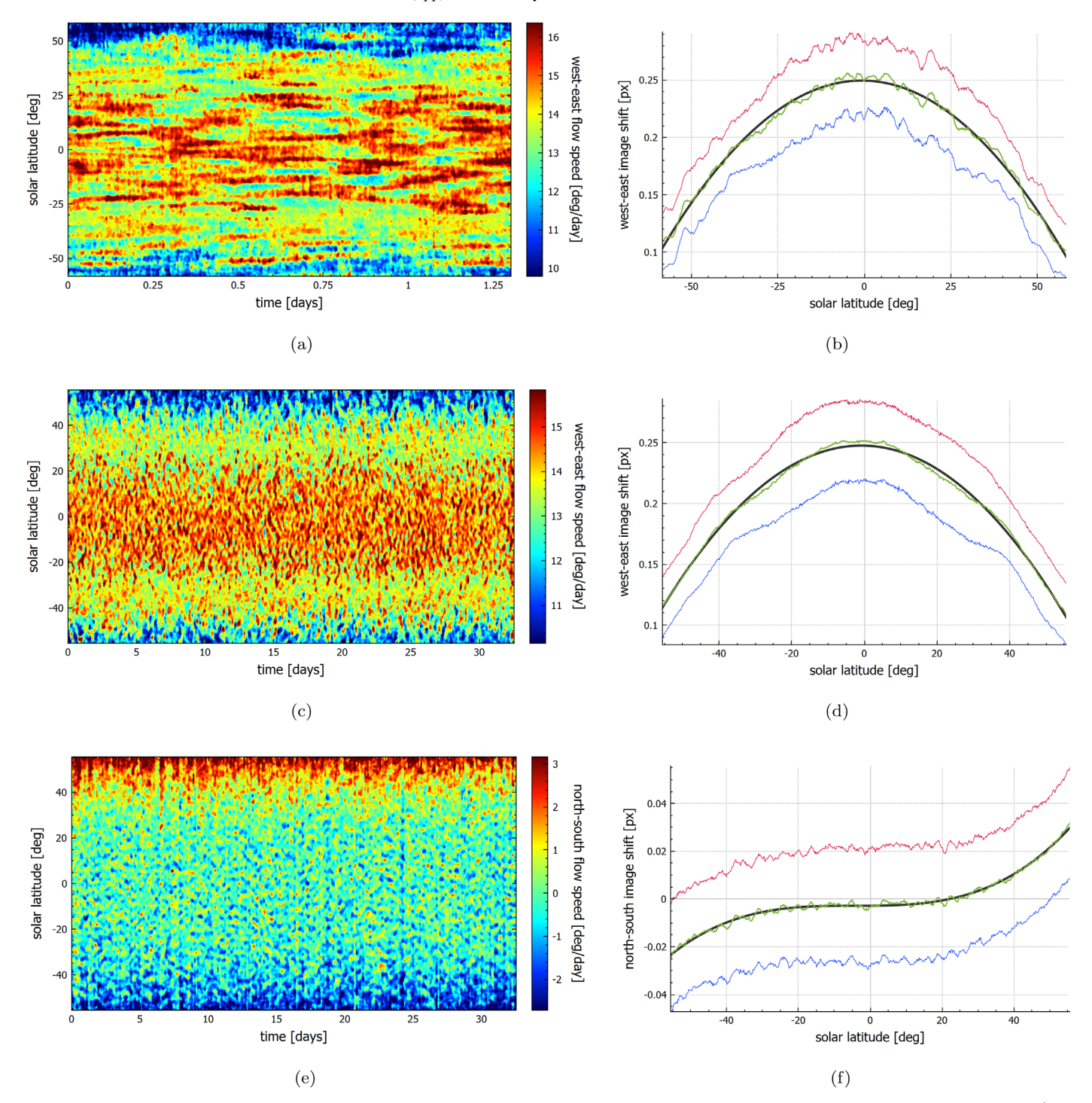


Figure 4. Solar west–east and north–south flow speed maps (left column) obtained from orthographically back-projecting image shifts measured on 2000 SDO/HMI continuum full-disk image pairs back onto the solar surface with the corresponding plots of the average image shift profiles (right column). Image shift calculations were done on uniformly distributed image pairs with  $\Delta t = 45$  s intervals between individual images in each pair. First row: west–east flow speed map (a) and corresponding average west–east image shift profile  $\overline{\Delta x}(\theta)$  (b) (green) obtained from images spanning approximately a one day period from 2020 January 1 to January 2, together with its best least-squares second degree polynomial fit curve (black) and one standard deviation band (blue, red). Second row: same as the first row for a one month period from 2020 January 1 to February 2. Third row: north–south flow speed map (e) and corresponding average north–south image shift profile  $\overline{\Delta y}(\theta)$  (f) (green) obtained from images spanning approximately a one month period from 2020 January 1 to February 2, together with its best least-squares third degree polynomial fit curve (black) and one standard deviation band (blue, red). Positive north–south values indicate southward flows, while negative values indicate northward flows.

followed by shifting the ROI toward the current centroid, converging to a high-precision subpixel solution.

To compare the IPC method with some other techniques, we examined three different approaches. Foroosh et al. (2002) used a different way to extend the method to subpixel accuracy,

which is analytical, with no iterative refinement. Takita et al. (2003) used least-squares 2D regression to fit the neighborhood around the maximum peak and then based the resulting image shift on the fit. Balci & Foroosh (2006) inferred the image shift directly from the frequency domain, counting the number of

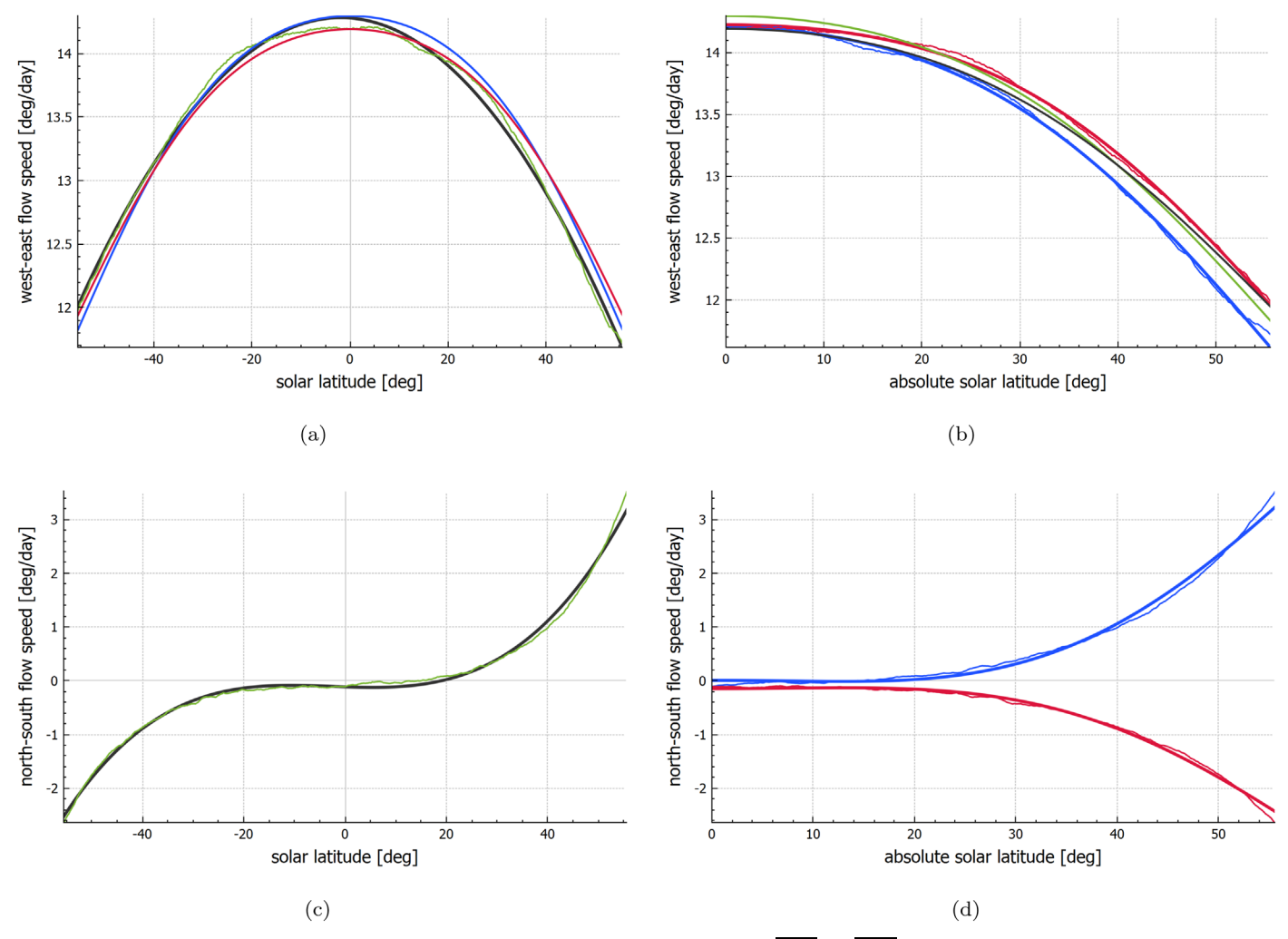


Figure 5. Average measured west–east (first row) and north–south (second row) flow speed profiles  $\overline{\omega_x(\theta)}$  and  $\overline{\omega_y(\theta)}$  at different latitudes in degrees per day. Measured from a one month period from 2020 January 1 to February 2. The flow speed profile was obtained by temporally averaging values at each latitude in the corresponding flow speed map (Figure 4(c)). Panels (a) and (c) contain the entire average west–east and north–south profiles (green) with their corresponding best least-squares second and third degree polynomial fits  $\omega_x^*(\theta)$ ,  $\omega_x^*(\theta)$  (black). Furthermore, two sample west–east trigonometric flow speed profiles inferred by different techniques (Howard et al. 1983; Lamb 2017) are also included (blue, red) in (a). Panels (b) and (d) contain the average measured west–east and north–south flow speed profiles with their corresponding best least-squares trigonometric fit curves  $\omega_x^{\dagger}(\theta)$ ,  $\omega_y^{\dagger}(\theta)$  for northern (blue) and southern (red) hemisphere separately at different absolute latitudes, together with the two sample west–east trigonometric flow speed profiles inferred by different techniques (green, black) in (b).

phase-difference sawtooth cycles, while calculating the subpixel part of the image shift from the fraction of the last (incomplete) cycle.

#### 4.2. The Equatorward Result

Most other techniques observe poleward flows at the surface and return equatorward flows beneath. However, there are also techniques which show the possibility of a circulation with a shallow equatorward return flow (e.g., Miesch et al. 2006; Guerrero et al. 2012; Käpylä et al. 2012; Zhao et al. 2013). Furthermore, this result could be connected with the well-established migration of active regions, which initially emerge at midlatitudes and appear at progressively lower latitudes as the cycle progresses, thus exhibiting equatorward migration.

Both image shift and flow speed profiles display equatorward flow, which eliminates the possibility of this result being caused by wrong geometric equations. The image shift and flow speed profiles are roughly symmetric around the origin, which also eliminates other systematic effects, like inaccurate center pixel coordinates from the FITS image header (these

 Table 2

 Polynomial Flow Speed Fit Coefficients

Flow Speed Curve Type	а	b	с	d
W–E (1 month)	14.28	-0.17	-2.58	•••
W–E (1 day)	14.34	-0.14	-2.38	
N–S (1 month)	-0.11	-0.18	0.47	3.31
N–S (1 day)	-0.17	-0.23	0.20	3.42

**Note.** The table includes best (least-squares) fitting coefficients *a*, *b*, *c*, *d* for different types of west–east (W–E) and north–south (N–S) polynomial flow speed profile fits (both hemispheres together), obtained from both one month and one day data sets in degrees per day according to Equations (13) and (14).

would cause the whole profile to be shifted up or down by an equal amount at each latitude in each picture pair and thus would not be able to cause the observed latitudinal variation). The authors leave the interpretation of this result to the broader scientific community.

#### 5. Summary and Conclusions

The novel iterative phase correlation technique of solar differential rotation estimation described and illustrated in this paper offers a new method for the empirical determination of the differential rotation rate of the solar photosphere. It is based on the measurement of locally varying image shifts between consecutive ( $\Delta t = 45 \, \mathrm{s}$ ) solar images. The technique was applied to SDO/HMI data and roughly covered one Carrington rotation of continuous observations from 2020 January 1 to February 2. The technique has a number of exceptional properties which make it superior to other correlation-based techniques, mainly in the domain of high spatial and temporal resolution.

The local shift measurement between two images is not limited to high-contrast features like sunspots, as it can be applied even to very low-contrast structures, such as granulation and/or faculae (see Figure 1). Hence, the differential rotation rate thus determined is independent of any a priori selection of solar features. Therefore the method can be successfully applied to any location in the photosphere and does not require long observations spanning months or years (see the results obtained by measurements from just one day in Figures 4(a) and (b)).

The very high temporal resolution of the presented method enables the study of short-period photospheric phenomena and the comparison of measurements on different days separated by an event that may have a global impact on the solar magnetic field, such as a solar flare or a coronal mass ejection. Furthermore, given that the technique does not rely on visible features, it can be used throughout a full solar cycle independently of the presence of specific features in the photosphere.

While methods based on solar markers yield a limited number of data points, the iterative phase correlation technique is applicable to every pixel close to the central meridian within a given latitude band. This yields a unique opportunity to study the rotation rate of the Sun locally.

The method is also able to estimate the locally varying north–south shifts between consecutive solar images. Although being very small and hard to measure (~0.01 pixel—see Figure 4(f)), the north–south image shifts obtained by the novel image registration method show coherent results, displaying a consistent global trend (see Figure 5(c)). The reliability of the north–south image shift measurement allows further studies of the general (not only rotational) photospheric movements with great detail. The north–south flow speed results show an overall flow toward the solar equator, with speeds becoming more significant closer to the geographic poles. Both the west–east and north–south flow speed profiles were fitted with polynomial and trigonometric curves, whose best (least-squares) parameters can be seen for both one day and one month observations in Table 1.

In conclusion, the reliability of the approach is underscored by the fact that the average sidereal differential rotation curve obtained is in the middle of other published results (see Figures 5(a) and (b)). At the same time it also clearly shows the now well-established N–S rotational speed asymmetry. Furthermore, the quality of the results is further supported by the smoothness of the average west–east image shift profile obtained from a single Carrington rotation of SDO/HMI image data (see Figure 4(d)) and also by the coherence of the measured flow speed values inferred from temporally adjacent images. As an added bonus, the novel technique described in this work allows the study of short-lived and previously undetected phenomena associated with the solar magnetic field.

The authors thank the anonymous reviewers for their careful reading of the manuscript and their many insightful comments and suggestions, which improved the manuscript quality.

The work of Z.H. and M.D was supported by the Grant Agency of Brno University of Technology, project No. FSI-S-14-2290. S.H.'s contribution was supported by NSF grant AGS-1834662 to the University of Hawaii.

## **ORCID iDs**

Zdeněk Hrazdíra https://orcid.org/0000-0001-7362-4947 Shadia Habbal https://orcid.org/0000-0003-4089-9316

#### References

```
Babcock, H. W., & Babcock, H. D. 1955, ApJ, 121, 349
Balci, M., & Foroosh, H. 2006, EJASP, 2006, 060796
Beck, J. G. 2000, SoPh, 191, 47
Druckmüller, M. 2009, ApJ, 706, 1605
Druckmüller, M., Habbal, S. R., & Morgan, H. 2014, ApJ, 785, 14
Elsässer, W. M. 1950, RvMP, 22, 1
Foroosh, H., Zerubia, J. B., & Berthod, M. 2002, ITIP, 11, 188
Guerrero, G., Smolarkiewicz, P., Kosovichev, A., & Mansour, N. 2012, in IAU
  Symp. 294, Solar and Astrophysical Dynamos and Magnetic Activity
  (Cambridge: Cambridge Univ. Press), 417
Howard, R., Adkins, J., Boyden, J., et al. 1983, SoPh, 83, 321
Hrazdíra, Z., Druckmüller, M., & Habbal, S. 2020, ApJS, 247, 8
Käpylä, P. J., Mantere, M. J., & Brandenburg, A. 2012, ApJL, 755, L22
Kuglin, C. D., & Hines, D. C. 1975, in Proc. IEEE Int. Conf. on Cybernetics
  and Society (Piscataway, NJ: IEEE), 163
Lamb, D. A. 2017, ApJ, 836, 10
Leibacher, J. W., Noyes, R. W., Toomre, J., & Ulrich, R. K. 1985, SciAm,
Leighton, R. B., Noyes, R. W., & Simon, G. W. 1962, ApJ, 135, 474
Lemen, J. R., Akin, D. J., Boerner, P. F., et al. 2011, The Solar Dynamics
  Observatory (Berlin: Springer), 17
Miesch, M. S., Brun, A. S., & Toomre, J. 2006, ApJ, 641, 618
Parker, E. N. 1955, ApJ, 122, 293
Scheiner, C. 1630, Rosa Ursina Sive Sol, book 4, part 2
Takita, K., Aoki, T., Sasaki, Y., Higuchi, T., & Kobayashi, K. 2003, IEITF,
  86, 1925
Thompson, M., Toomre, J., Anderson, E., et al. 1996, Sci, 272, 1300
Zhang, L., Mursula, K., & Usoskin, I. 2015, A&A, 575, L2
Zhao, J., Bogart, R., Kosovichev, A., Duvall, T., Jr, & Hartlep, T. 2013, ApJL,
  774, L29
```